ELSEVIER

International Journal of Solids and Structures 41 (2004) 3521–3543

INTERNATIONAL JOURNAL OF SOLIDS and STRUCTURES

www.elsevier.com/locate/ijsolstr

Design and demonstration of a high authority shape morphing structure

S.L. dos Santos e Lucato *, J. Wang, P. Maxwell, R.M. McMeeking, A.G. Evans

Materials Department, Mechanical Engineering Department, University of California at Santa Barbara, Santa Barbara, CA 93106, USA

Received 25 July 2003; received in revised form 27 January 2004
Available online 12 March 2004

Abstract

A concept for a high authority shape morphing plate is described and demonstrated. The design incorporates an active back-plane comprising a Kagome truss, capable of changing the shape of a solid face, connected to the back-plane by means of a tetrahedral truss core. The two shape deformations to be demonstrated consist of hinging and twisting. The design is performed by a combination of analytic estimation and numerical simulation, guided by previous assessments of the Kagome configuration. It is shown that, while the structure is capable of sustaining large passive loads at low weight, the demonstrable authority is actuator-limited. The full potential of the system can only be realized by developing and incorporating superior actuators.

An optimization has been used to ascertain the largest displacements achievable within the force capability of the actuators. These displacements have been demonstrated and shown to correspond with values predicted by numerical simulation. The consistency between measured and calculated responses has allowed objectives to be set for alternative materials, as well as structural and actuator enhancements.

Keywords: Shape morphing; Sandwich panels; Actuator; Optimization; Failure mechanisms

1. Introduction

One of the goals in shape morphing technology is to cause surfaces to displace even when resisted by large pressure loads (or heavy weights). The challenges become especially demanding when minimum weight requirements and power budgets are imposed. This challenge can be addressed by seeking structures that are simultaneously statically determinate, yet stiff. A two-dimensional manifestation consists of a corrugated structure that can bend and hinge with much higher authority than bimorphs and other competing approaches (Lu et al., 2001). Another manifestation is the Kagome structure depicted on Fig. 1 (Hutchinson et al., 2003; Hyun and Torquato, 2002), having the attribute that it can be actuated into intricate surface shapes, ranging from bending to twisting to undulating (Fig. 2). The basic mechanics have

* Corresponding author. Tel.: +1-805-8934341; fax: +1-805-8938486.
E-mail address: lucato@engineering.ucsb.edu (S.L. dos Santos e Lucato).

0020-7683/$ - see front matter © 2004 Elsevier Ltd. All rights reserved.
doi:10.1016/j.ijsolstr.2004.02.012

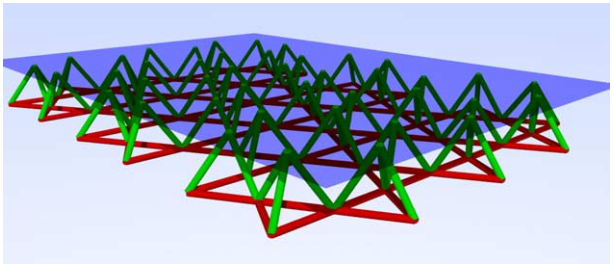

Fig. 1. Schematic representation of the Kagome-structure. The face-sheet is shown in blue, the core in green and the Kagome back-face is red.

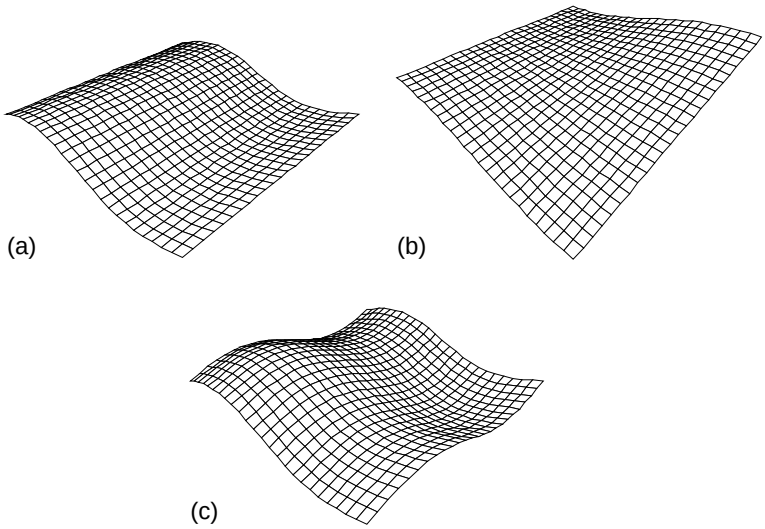

Fig. 2. Target surface shapes ranging from bending (a) to twisting (b) to undulating (c).

been elucidated elsewhere (Hutchinson et al., 2003). The intent of the study is to provide an experimental assessment of the concept with associated analysis. For this initial demonstration, hinging and twisting will be explored. The more complex contours depicted on Fig. 2 will be demonstrated in future assessments. The design process selects the geometry and the preferred materials. It ascertains the stresses, relative to the failure envelope, and ascertains the actuator authority needed to maximize the load capacity as a function of the designated displacements.

The basic structural design is depicted on Fig. 3. It consists of a solid face-sheet with a Kagome back-plane and a tetrahedral core. A related design based on two Kagome faces and a tetrahedral core is described elsewhere (Symons et al., 2003). The length of the panel is chosen to include six hexagonal units of the Kagome plate, while the width incorporates four units with member length, $L = 5.1$ cm. Along the sides, to avert degradation of the buckling resistance, patch trusses are used. For initial demonstration, the back-plane and core members have the same length and cross-section. Future demonstrations will use selected members with differing cross-section. The configuration is rigidly supported at one end. Replacing various truss elements in the back-plane with linear actuators enables the shape of the solid face to be changed. To achieve smooth contour changes and low structural weight, the solid face and the back-plane are stiffness matched (Christensen, 2000, Wicks, 2003). For the actual demonstration, the length of the panel is chosen

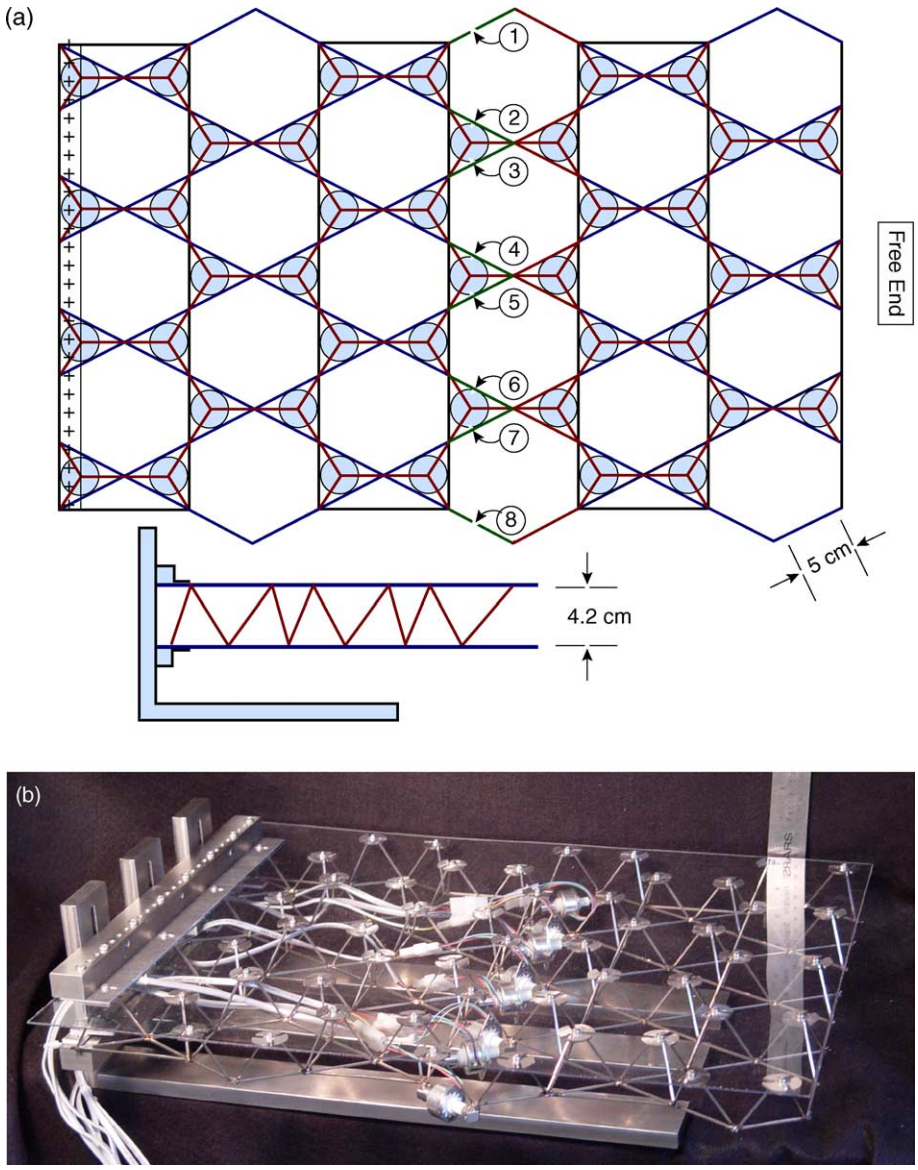

Fig. 3. Final assembly of Kagome-structure with actuator positions highlighted. Design (a) including the fixture and photo (b).

to include six hexagonal units of the Kagome plate, while the width incorporates four units. The truss aspect ratio has been chosen to maximize the displacement without failure, as described below. The objectives are to demonstrate hinging and twisting displacements, subject to large pressures and static end loads.

To facilitate fabrication, the Kagome and tetrahedral structures are fabricated from 304 stainless steel by laser cutting, followed by bending, as described elsewhere (Maxwell et al., 2003). This material choice limits the shape morphing performance because of its low yield strain, $\varepsilon_Y = 10^{-3}$, and high density. The enhanced performance to be realized upon using Ti or Al alloys (having higher yield strain and lower density) will be emphasized. The core members incorporate circular pads, which facilitate attachment to the solid face. The

attachment is performed by welding, but could be created by transient liquid phase (TLP) bonding or, in the case of Ti, by diffusion bonding.

For morphing purposes, various truss elements are replaced by linear actuators. The replacements are made in pairs (Fig. 3), to minimize local distortions. A commercial linear, stepper actuator (Haydon Switch, model Z 26443) is used. This actuator can extend to strains $>10\%$, but can only displace loads of 50 N at a stepping rate of 50/s decaying linearly to 1 N at 700/s. This operating characteristic limits the passive loads that can be supported, as elaborated below, highlighting the need for a higher authority actuator. Accordingly, the test results and the analysis will be used for two additional purposes.

(i) Evaluate the loads on the actuator that could be lifted upon incorporating actuators with superior force capability.
(ii) Define the actuator capabilities that would be needed to create a structure-limited rather than actuator-limited system.

The design is achieved by a combination of analytic approximations with more detailed finite element results. The procedure has two steps. *Step I.* Analytic results for the stresses caused by passive loads are derived using beam and plate theory. These results are used to estimate dimensions and to assess the scaling. They are augmented by selected finite element calculations. *Step II.* The stresses and displacements induced during actuation are determined using finite elements, with emphasis on the core and face members adjacent to the actuators. The same calculations are used to evaluate the forces on the actuators as a function of the displacements. At this stage, the dimensions are adjusted and the load capacity re-evaluated to assure that there is no cyclic yielding (indicative of fatigue) or buckling.

Numerical simulations depicted on Fig. 4 illustrate the shape changes to be explored.

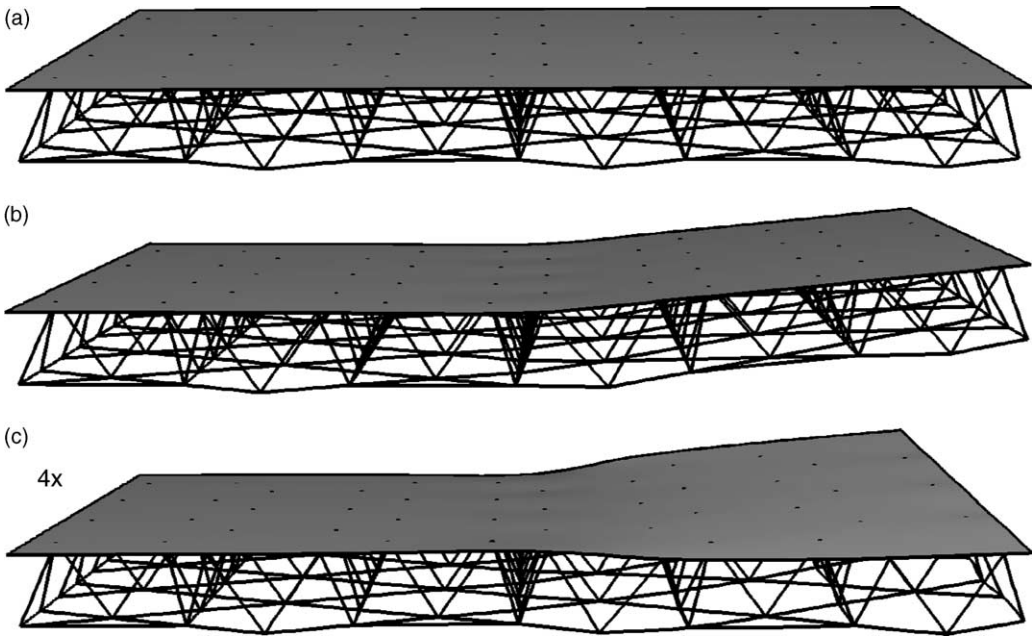

Fig. 4. Numerical results for hinging and twisting modes of the Kagome structure. (a) Initial configuration. Resulting shapes of hinging (b) and twisting (c) modes.

2. Numerical procedures

A finite element method has been used for several purposes:

(i) To generate results that can be compared with analytic solutions governing the passive loads.
(ii) To calculate the stresses induced by actuation, for twisting and hinging deformations, and to ascertain the forces on the actuators.
(iii) To determine the actuator displacements that achieve a prescribed displacement of the solid face sheet, consistent with a minimum in the largest load experienced by any of the actuators.

The calculations are conducted at two different levels, by using the finite element package ABAQUS. *To simulate the complete system*, the core and the Kagome face members are modeled using linear Timoshenko-type beams, while the solid face sheet is discretized using general-purpose shell elements. A total of 10 elements are used per member to capture bending and buckling. The actuators are incorporated into the model by means of truss elements, with representative cross-sectional area. One side of the structure is clamped. Actuation is achieved by changing the temperature of the truss elements representing the actuators. The passive response is assessed by applying a line load along the outer edge of the solid face sheet.

A full *elastic/plastic analysis is performed on the following two sub-systems* by using 3D solid elements. (a) The in-plane performance of the Kagome is evaluated and compared with existing results. Imperfections are introduced into the truss members to assure that elastic and plastic buckling effects are captured. (b) The core tetrahedron above the actuators is found to be most susceptible to cyclic yielding during actuation. To find materials and configurations that obviate this potential problem, a single tetrahedron is modeled. For this purpose, two of the members are clamped and cyclic displacements imposed on the third member with amplitude ascertained from the system-level model.

3. Passive load capacity

3.1. The back-plane design

The Kagome back-plane is designed by balancing the in-plane failure mechanisms, using the unit cell loci depicted on Fig. 5. The non-dimensional coordinates characterizing yielding are (Hutchinson et al., 2003)

$$\begin{aligned} \Pi_{11} &\equiv N_{11} L_{\mathrm{f}} / A_{\mathrm{f}} \sigma_{\mathrm{Y}}, \\ \Pi_{22} &\equiv N_{22} L_{\mathrm{f}} / A_{\mathrm{f}} \sigma_{\mathrm{Y}}, \end{aligned} \tag{1}$$

where N_{ii} refers to the in-plane load per unit length, L_{f} is the length of the truss members, A_{f} is their cross-sectional area and σ_{Y} is the yield strength of the material to be used. The present demonstration uses trusses with square cross-section, d_{f} ($A_{\mathrm{f}} = d_{\mathrm{f}}^2$). To characterize buckling, the additional non-dimensional parameter is (Hutchinson et al., 2003)

$$\Sigma = \sqrt{I_{\mathrm{f}}/A_{\mathrm{f}}} / L_{\mathrm{f}} \sqrt{\varepsilon_{\mathrm{Y}}}, \tag{2}$$

where I_{f} is the moment of area of the truss members and ε_{Y} is their yield strain. Each buckling contour on Fig. 5 refers to a particular choice of Σ.

Since the optimal performance of structures often occurs at the confluence of failure mechanisms (Ashby et al., 2000), it is assumed that the maximum actuation displacement without failure occurs when the slenderness ratio of the trusses in the Kagome face is coincident with simultaneous failure by buckling and yielding (see Fig. 8). A more complete assessment is described elsewhere (Wicks and Hutchinson, 2001; Hutchinson et al., 2003). For the uni-axial deformations envisaged in the current demonstration ($N_{22} = 0$), the failure mechanisms are simultaneous when (Fig. 5)

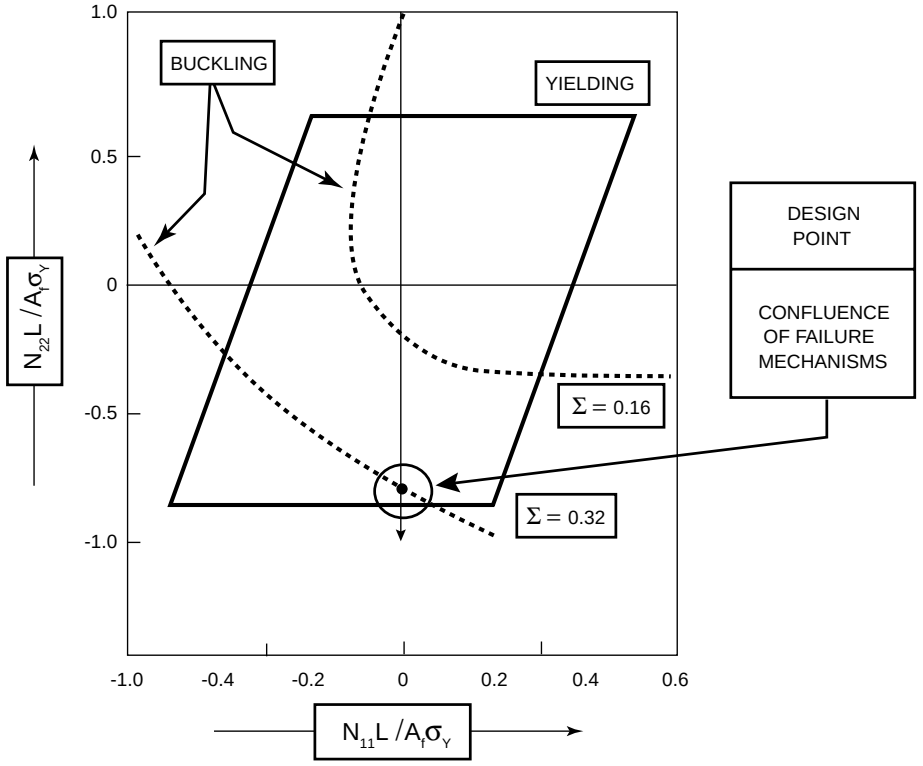

Fig. 5. In-plane failure mechanisms of the Kagome back-plane. Loads exceeding the shaded region result in failure by yielding. The dashed curves represent the load-limits established by buckling.

$$\Sigma \approx 0.32, \tag{3a}$$

$$\Pi_{11} = 0.866. \tag{3b}$$

As elaborated below, the patched topology (Fig. 3) has a greater buckling resistance than implied by Fig. 5. Accordingly, imposing condition (3) causes failure by yielding in preference to buckling. Future demonstrations will take account of this extra buckling resistance.

Condition (3a) determines the aspect ratio of the trusses as (Hutchinson et al., 2003)

$$d_f/L_f = 1.1\sqrt{\varepsilon_Y}. \tag{4}$$

Evidently, the design depends on the choice of alloy, through ε_Y. For the present demonstration, performed using 304 stainless steel ($\sigma_Y = 200$ MPa, $\varepsilon_Y = 10^{-3}$), the preferred truss aspect ratio is: $L_f/d_f = 29$. Such a design would be yield-limited as noted above. The corresponding ratio for alloys with higher yield strain would be smaller: for example, a structure made using a Ti–6V–4Al alloy ($\sigma_Y = 800$ MPa, $\varepsilon_Y = 6.10^{-3}$), would correspond to an aspect ratio: $L_f/d_f \approx 13$. Additional considerations based on the overall weight might change this choice of aspect ratio.

The maximum value of the nominal in-plane stress ($\sigma_{11} = N_{11}/d_f$) that can be sustained by the trusses is obtained from (3b) and (4) as

$$\Sigma^{max} \equiv \sigma_{11}^{max}/\sigma_Y = 0.866(d_f/L_f) \equiv 0.95\sqrt{\varepsilon_Y}. \tag{5}$$

Now the benefits of the Ti alloy over stainless steel become especially apparent. For stainless steel, $\Sigma^{max} = 3.48 \times 10^{-3}$ and $\sigma_{11}^{max} = 0.7$ MPa. For Ti alloys, these loads are much larger: $\Sigma^{max} = 7.78 \times 10^{-3}$ and

$\sigma_{11}^{max} = 6.2$ MPa. The stress σ_{11}^{max} provides a bound on the passive load that can be realized, as well as bounding the largest allowable actuation strain.

Selected numerical results for the response of the Kagome are summarized on Figs. 6 and 8. They refer to responses induced when displacements are imposed in the one-direction. The calculations are performed with and without imperfections and assessed with and without yielding. They are conducted in accordance with stress/strain characteristics representative of 304 stainless steel. Results are presented for two cases: yield control (Fig. 6(a)), and buckling control (Fig. 6(b)). When yielding is preceded by buckling (Fig. 6(b)), it occurs in strict accordance with Fig. 5. In the presence of imperfections, it is immediately followed by plastic buckling, with rapid softening, attributed to the slenderness of the truss members. When susceptible to elastic buckling (Fig. 6(b)), and when imperfections are present, bending of the truss members once they buckle, causes them to yield, with resultant softening. In the presence of patches, the effective stress at buckling (Fig. 7) exceeds that expected from the periodic model (Fig. 5). Omitting the patches reduces the buckling stress to a level below that in Fig. 5, highlighting the beneficial role of patch members in governing the overall performance.

3.2. The load capacity

The magnitudes of the passive loads that can be supported without failure are derived for a cantilever plate with a line load, P (per unit width) imposed at the free-end (Fig. 3). Emphasis is placed on analytic formula that can be used to select materials and to assess the scaling. A complete analysis, presented elsewhere (Wicks and Hutchinson, 2001) (Fig. 8), reveals that when optimized, this design is as good as the best available truss structures and competitive with honeycomb core panels. In loadings that cause the solid face to experience compression, it fails by local buckling, requiring that this face be relatively thick. The consequence is a minimum weight design comparable to that for the octet truss (Deshpande and Fleck, 2001). For loads that allow the face to remain in tension, as in the present demonstration, the structure is lighter, with weight comparable to that for a fully optimized sandwich panel (Wicks and Hutchinson, 2001). Moreover, when optimized, the face has about the same stiffness as the active Kagome face. Failure occurs by simultaneous yielding and buckling of both the Kagome face and the core.

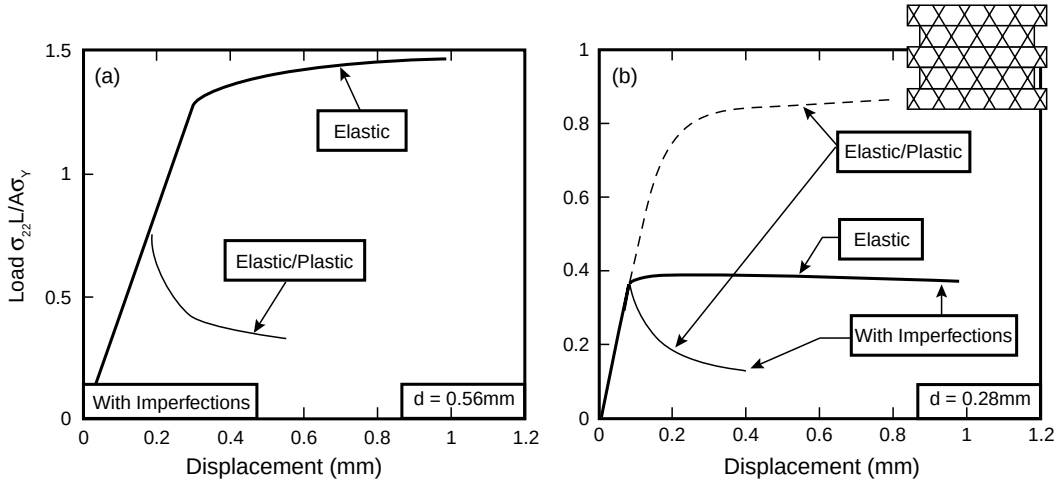

Fig. 6. Numerical results for the load-displacement responses of the Kagome back-plane subject to uniaxial in-plane straining. Results are presented for two cases: one wherein the structure is expected to be yield-controlled (a) and another when buckling-controlled (b).

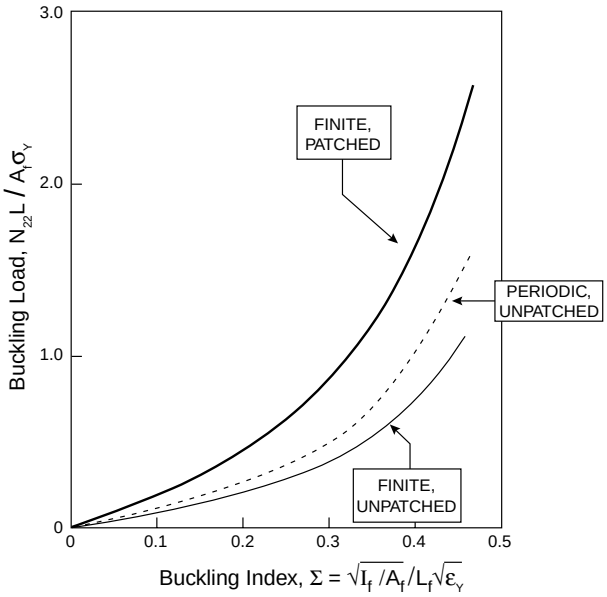

Fig. 7. In-plane buckling load of the Kagome back-plane depicted for an infinite, periodic structure, compared with a finite, unpatched structure, as well as a finite, patched structure.

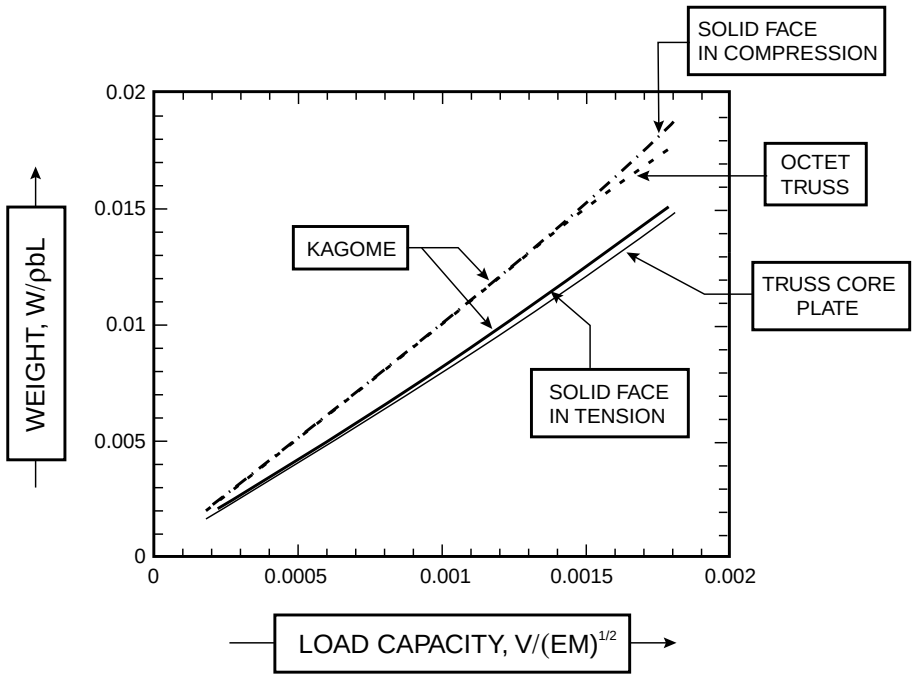

Fig. 8. Minimum weight as a function of the load-capacity for several sandwich panel geometries (Wicks, 2003). Note that the Kagome structure performs as well as the best available truss structures.

(i) *The back-plane load capacity*. The Kagome back-plane and the solid face must sustain the bending moment. Since these faces are stiffness matched, the nominal stress induced in the back-plane is related to the bending moment, M, by (Ashby et al., 2000)

$$\sigma_{11} = M/d_f H_c, \tag{6a}$$

where H_c is the core thickness. For the present case, wherein the core and face truss members have the same dimensions (this will be a variable in future assessments), $L_c = L_f$, (6a) becomes

$$\sigma_{11} = \sqrt{3/2}Ps/d_f L_f, \tag{6b}$$

where s is the span (Fig. 3). Since the aspect ratio has been chosen to assure failure by yielding rather than buckling, equating σ_{11} to σ_{11}^{max} (5) gives the end load that can be supported without failing the faces by yielding as

$$P_M \leqslant 0.866\sqrt{2/3}\frac{d_f^2}{s}\sigma_Y. \tag{7}$$

(ii) *Passive face*. When the passive face is stiffness matched to the back-plane, its thickness, d_{pf} would be

$$\frac{d_{pf}}{d_f} = \frac{E}{E_{pf}}\frac{d_f}{\sqrt{3}L_f} \equiv \frac{1.1\sqrt{\varepsilon_Y}}{\sqrt{3}}\frac{E}{E_{pf}}, \tag{8}$$

where E_{pf} is the Young's modulus of the face. For the present demonstration, polycarbonate is used for the face ($E_{pf} = 4$ GPa), whereupon, $d_{pf} \approx d_f$. Much smaller face thickness would be required when a metal face is used. For example, an Al alloy face would require that, $d_{pf}/d_f = 0.13$.

The load that can be supported by the faces prior to yield, in a stiffness-matched system, is given by (Wicks and Hutchinson, 2001)

$$P_M^f \leqslant \sqrt{2/3}\sigma_Y^f d_{pf} L_f/s, \tag{9}$$

where σ_Y^f is the yield strength of the face. The ratio of the loads that can be sustained by the face and the back-plane is thus

$$\frac{P_M^f}{P_M} = 0.67\frac{\varepsilon_Y^f}{\varepsilon_Y}. \tag{10}$$

For a polycarbonate face ($\varepsilon_Y^f \approx 1.5 \times 10^{-2}$) and stainless steel back-plane ($\varepsilon_Y \approx 10^{-3}$), the load capacity is limited by yielding of the back-plane. When the passive face and the back-plane are made from the same material, the structure would be limited by face yielding. Small thickness adjustments would change this tendency.

In normal operation, the passive loads place the faces in tension. However, should the design require the face to experience compression, it would be susceptible to wrinkling, which would occur in accordance with

$$P_{Mw}^f \leqslant \sqrt{3/2} \times 2.24 E_{pf}\frac{d_{pf}^3}{L_f}. \tag{11}$$

The ratio of the wrinkling load to the yield load is

$$\frac{P_{Mw}^f}{P_M^f} = \frac{3.36}{\varepsilon_Y^f}\left(\frac{d_{pf}^3}{d_f L_f^2}\right). \tag{12}$$

This ratio reveals that face failure will occur preferentially by wrinkling, which accounts for the effects of loading direction expressed in Fig. 8.

(iii) *Load supported by the core*. The tetrahedral core must sustain the shear force without yielding or buckling. The end load that can be supported by core members with square cross-section, before yielding, is given by (Wicks and Hutchinson, 2001)

$$P_{\mathrm{v}} \leqslant \frac{1}{\sqrt{6}} \frac{d_{\mathrm{c}}^2}{L_{\mathrm{c}}} \sigma_{\mathrm{Y}}. \tag{13}$$

(Note that this core has half the number of tetrahedral element as a truss core sandwich panel (Hutchinson et al., 2003)). The equivalent result for elastic buckling is

$$P_{\mathrm{Vb}} \leqslant \pi \frac{k E_{\mathrm{c}} d_{\mathrm{c}}^4}{4\sqrt{6} L_{\mathrm{c}}^3}, \tag{14}$$

where E_{c} is Young's modulus and k is a coefficient that depends on the end constraints (typically, $k \approx 1$). Comparing (13) and (14) and by using (4) for the aspect ratio of the core members, the ratio of the yielding and buckling loads becomes

$$\frac{P_{\mathrm{v}}}{P_{\mathrm{Vb}}} = \frac{4}{1.2k\pi}. \tag{15}$$

Accordingly, when $k \approx 1$, the core is essentially at the transition between yielding and buckling, which is desirable from a minimum weight perspective (Fig. 8) (Wicks and Hutchinson, 2001). A design with a core member thickness slightly larger than the face member thickness would assure failure by yielding.

(iv) *Overall load capacity*. When the core is yield-controlled (13), the ratio of the load capacity of the core and the back-plane is

$$\chi_{\mathrm{c}} \equiv \frac{P_M}{P_{\mathrm{V}}} = 1.74 \left(\frac{d_{\mathrm{f}}}{d_{\mathrm{c}}} \right)^2 \frac{L_{\mathrm{c}}}{s}. \tag{16}$$

At the optimum, $\chi_{\mathrm{c}} \approx 1$ (Wicks, 2003). The present design ($s/L_{\mathrm{c}} = 5.3$), with back-plane and core members having the same cross-section, is sub-optimal ($\chi_{\mathrm{c}} \approx 0.32$): whereupon the loads are limited by yielding of the back-plane. Accordingly, (7) can be used to estimate the passive load capacity as, $P_M \approx 1.2$ kN/m (equivalent to a load of 20 kg). Note that, replacing stainless steel with a Ti alloy ($\sigma_{\mathrm{Y}} = 800$ MPa) should increase the load capacity by a factor four: $P_M \to 4.8$ kN/m.

4. Actuation

Because of the bonded nature of the structure (Fig. 3), forces are induced upon imposing an actuation strain that can cause the system to be actuator-limited, rather than structure-limited. Before embarking on a shape morphing demonstration, it is essential to evaluate these forces and compare them with the operating characteristics of the actuator. Results are presented for actuators placed along the mid-section, half way between the support and the free end of the cantilever (Fig. 3), for the two scenarios outlined above. For hinging, all of the actuators are imparted the same extension (Fig. 4(b)). For twisting, different extensions are imposed on each actuator in the sequence described below (Fig. 4(c)).

4.1. Hinging

Resistance of the structure. Preliminary results for hinging displacements (Fig. 9) provide an indication of the resistance of the structure to actuation, expressed through the magnitudes of the forces on the actu-

ators, F_A, relative to those associated with the passive loads. The calculations also reveal that F_A is largely governed by the bending deformations induced in the core members and the face-plate immediately above the actuators. Accordingly, the scaling should have the form presented in Appendix A, which can be generalized as

$$\Sigma = \frac{1 + A(E_{pf}/E_c)\alpha + B(E_{pf}/E_c)^2\alpha^2}{C + D(E_{pf}/E_c)\alpha}, \tag{17a}$$

where Σ is the non-dimensional force

$$\Sigma = \frac{F_A L_c^3}{E_c \Delta d_c^4}, \tag{17b}$$

and α is a slenderness index

$$\alpha = \left(\frac{d_{pf}}{d_c}\right)^3 \frac{w}{d_c}. \tag{17c}$$

Here Δ is the actuator displacement, w is the width of the panel and A, B, C, D represent non-dimensional coefficients. The fidelity of this representation is ascertained by performing full numerical calculations of F_A for realistic ranges of the dimensions, with representative elastic properties (stainless steel, Ti and Al) and displacements (an actuation strain up to 10%). Results are obtained for steel and PMMA face sheets.

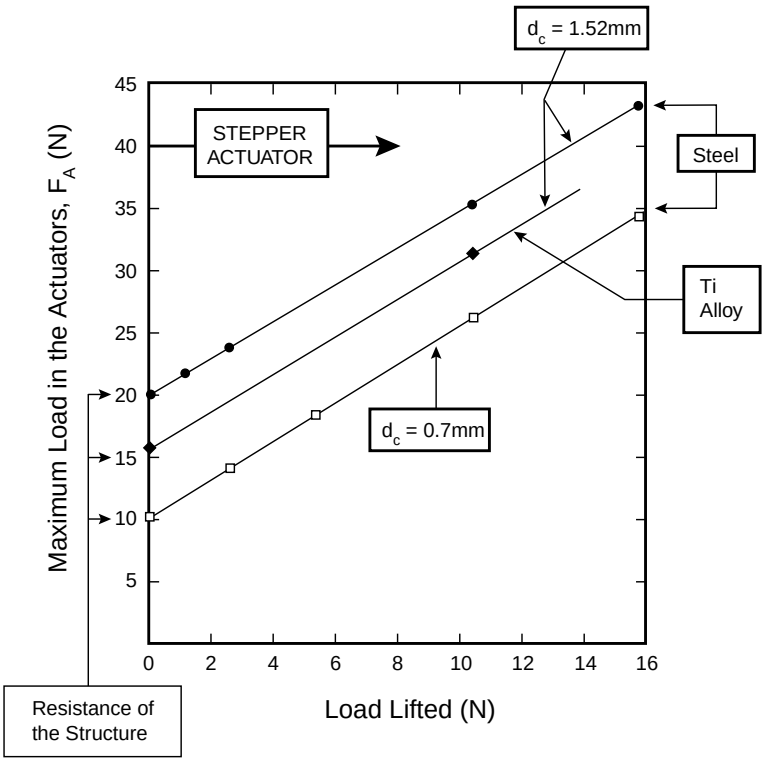

Fig. 9. Force on the actuators as function of the externally applied load. The resistance of the structure to actuation is obtained at zero external load.

To assess the relevant range, the dimensions that arise when the Kagome back-plane and the solid face are stiffness matched is determined as

$$\frac{d_c^2}{d_{pf}L_c}\frac{E_c}{E_{pf}} = \sqrt{3}. \tag{18}$$

Please note that the length and cross-section of the core members and the Kagome back-plane members are identical in this analysis. This implies that, for demonstrations similar to that in this article, for steel face sheets, $0 < \alpha < 0.02$, while for polycarbonate, $0 < \alpha < 2500$. Results have been obtained in these ranges (Fig. 10(a)–(d)) for core and Kagome face members having the same dimensions. The results for steel faces with *bonded joints* can be expressed as ($E_{pf} = E_c$)

$$\Sigma \approx 0.2 - 0.8\alpha + 13\alpha^2. \tag{19a}$$

The corresponding result when *the joints are pinned is*

$$\Sigma \approx 0.03\alpha. \tag{19b}$$

The result for polycarbonate faces bonded to the core ($E_c/E_{pf} = 1/200$) is

$$\Sigma \approx 0.22 + 6.2 \times 10^{-4}\alpha - 7.8 \times 10^{-8}\alpha^2. \tag{19c}$$

The large difference between (19a) and (19b) reinforces the major benefits of a pin-jointed design. Note that (19a) is relatively insensitive to α, signifying that the *steel faces* exert a minor contribution to F_A: whereupon, to a reasonable approximation, for bonded joints

$$F_A \approx 0.2E_c d_c (d_c/L_c)^3 \Delta. \tag{19d}$$

The crucial influence of the slenderness of the core members on F_A is apparent. Conversely, when *polycarbonate faces* are used, there is a strong α influence, such that the force on the actuator can be approximated by

$$F_A \approx 6.2 \times 10^{-4} E_c w (d_{pf}/L_c)^3 \Delta. \tag{19e}$$

That is, the force is dominated by the faces, so that reducing the core member thickness has a much smaller effect, as apparent from Fig. 9. The force on the actuator can thus be affected by the choice of face sheet material, with the non-intuitive trend that the *higher the material modulus, the lower the force* (because stiffness matching has been imposed). This finding is made explicit on Fig. 10(d), which compares actual values of F_A for steel and polycarbonate faces for two different assumptions. In one case the face and core members have the same thickness, consistent with Fig. 10(a)–(c). In the other, only the core member thickness is changed, consistent with Fig. 9. The latter demonstrates the large difference in F_A between the steel and polycarbonate faces, especially for slender cores.

The force on the actuators induced by the passive load, F_A^* can be obtained directly from (5) and (6) upon noting that the stress at the location of the actuators is half that at the supports

$$F_A^* = 0.58\sqrt{3/2}P_M s. \tag{20}$$

These two forces are additive, giving the result plotted on Fig. 9 for the present demonstration. It is apparent from these formulae and from Fig. 9 that the *forces on the actuators when the passive loads attain their maximum realizable magnitudes* (7) *far exceed the loads associated with the resistance of the structure*. To enable the system to become actuator dominated, the force capacity of the actuators would need to be increased to, $F_A \approx 300$ N for a steel system and, $F_A \approx 1200$ N for a Ti system.

Fatigue of the core members. The bending of the core members just above the actuators suggests that these may be susceptible to fatigue. To assess this possibility, a cyclic FEM analysis has been performed using the mesh depicted on Fig. 11(a). The analysis has been performed using stress/strain behaviors

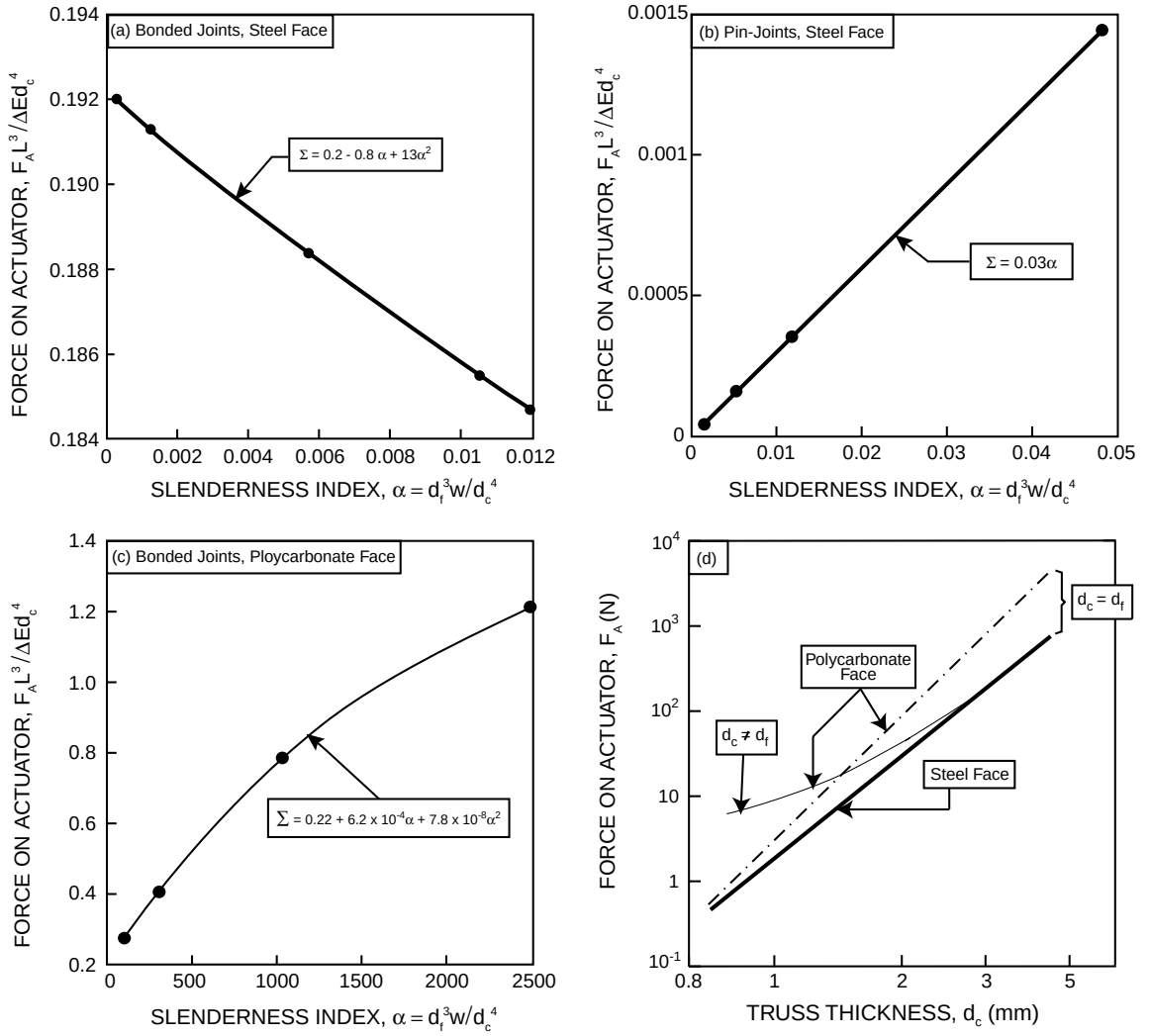

Fig. 10. The non-dimensional force on the actuators as function of the member slenderness. Results for a steel face are plotted for bonded joints (a) as well as flexible joints (b). Results for a polycarbonate face are plotted for bonded joints (c). Absolute values of the forces for steel and polycarbonate faces are compared (d) for several choices of the core member dimensions.

representative of both 304 stainless steel and Ti–6V–4Al. The calculations are performed by imposing prescribed displacements on the ends of the truss members ascertained from the full panel-scale model, actuated by a strain of 10%. The tab is allowed to displace freely in the vertical and horizontal directions. The first calculations have been performed for core members having the same slenderness as the face members. The largest bending stresses are located in the truss members adjacent to the tabs (Fig. 11(b)). For stainless steel, these stresses exceed the yield strength (Fig. 12(a)) resulting in cyclic plastic straining. While after about 40 cycles the system becomes elastic, indicative of shakedown, the response suggests a susceptibility to low cycle fatigue (LCF). In an attempt to obviate this problem, calculations have been

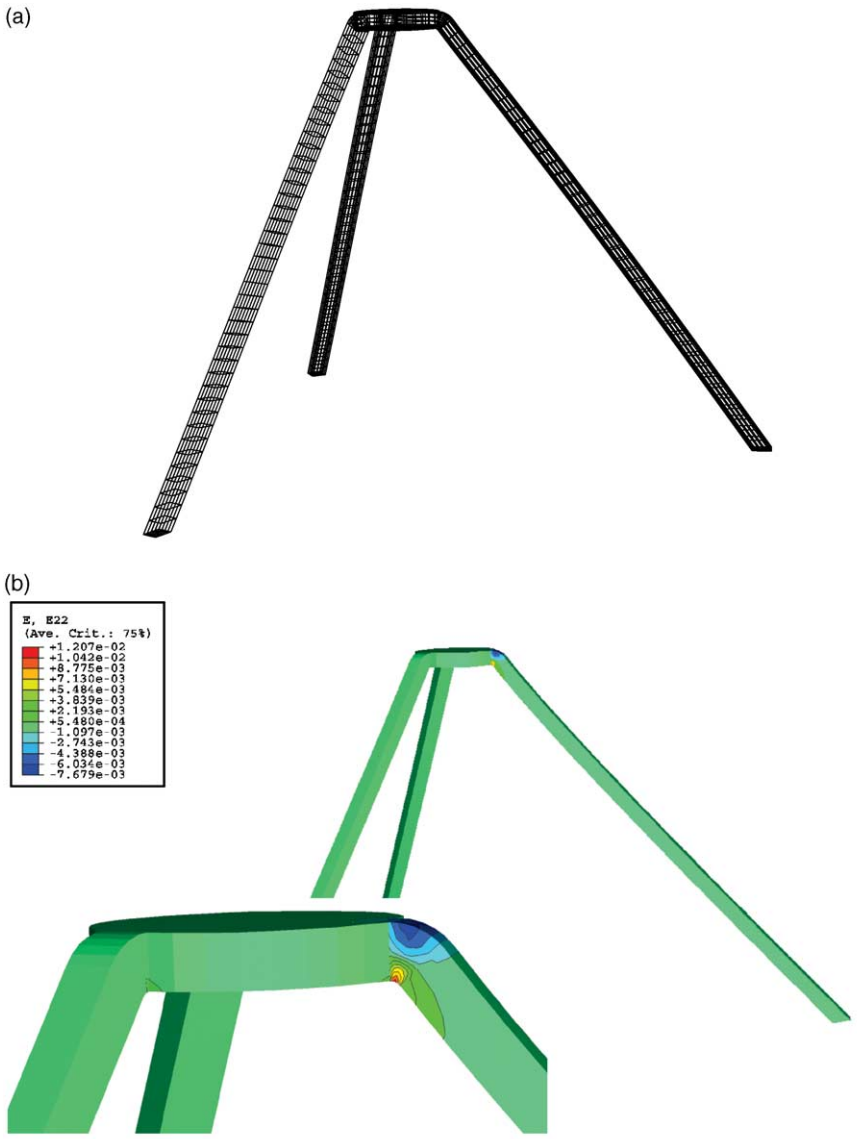

Fig. 11. Detailed fatigue study of a single core member. (a) FEA mesh. (b) Strains in the core member after 12 cycles.

performed for more slender core members: exemplified by the result for $d_c = 0.75$ mm (Fig. 12(b)). The modified results indicate that, when $d_c < 0.8$ mm, shakedown occurs after the first cycle (Fig. 12(b)) enabling the core members to be LCF resistant. To completely eliminate plastic deformation, further calculations reveal that the truss members need to be in the range, $d_c < 0.35$ mm. Such small values would diminish the passive load capacity, because of core buckling. The results for the Ti alloy (Fig. 12(c)) demonstrate the major advantages of this material, relative to stainless steel. Note that, even when the members are relatively thick, $d_c = 3$ mm, they remain elastic, eliminating LCF and alleviating high cycle fatigue (HCF).

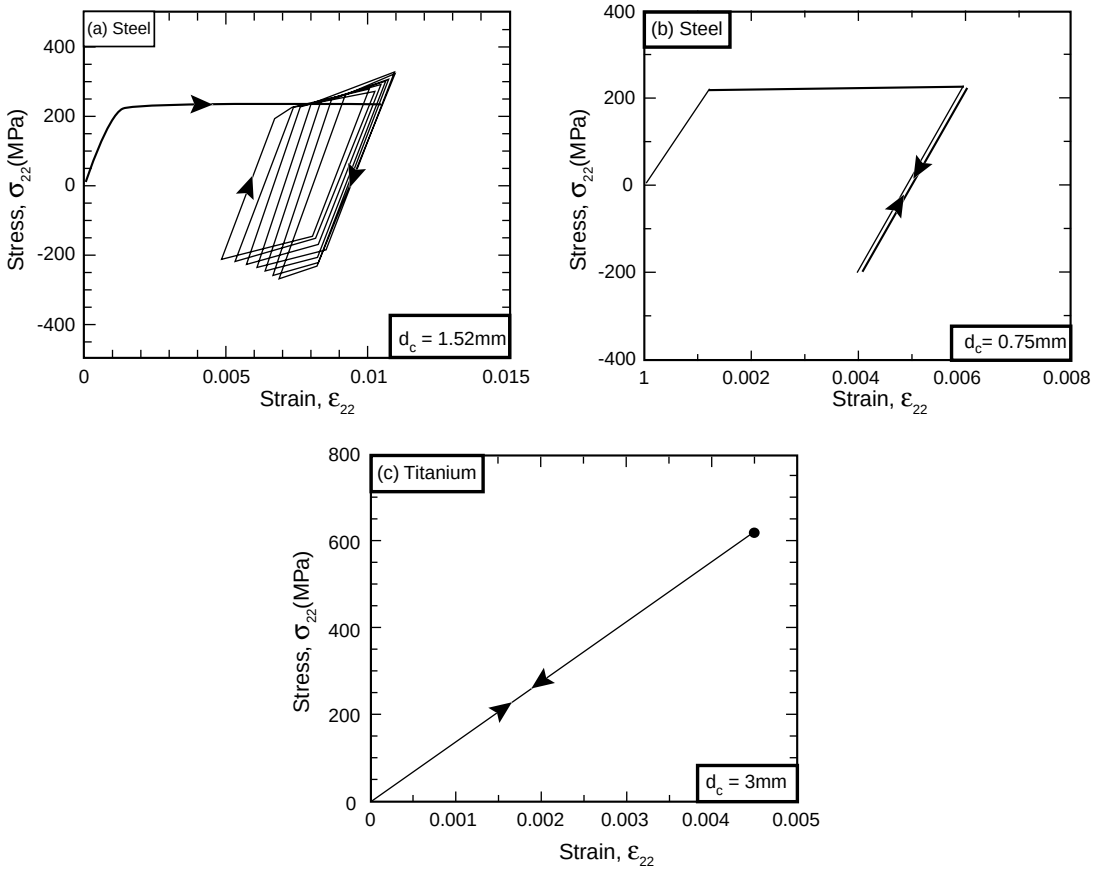

Fig. 12. Cyclic stress-strain curves at the maximum strain location calculated for core members fabricated from steel and titanium. Steel cores with a cross-section of 1.54×1.54 mm (a) and 0.7×0.7 mm (b): titanium core with a cross-section of 3×3 mm (c). Note that the titanium core members are 60 mm long while the steel core members are 51 mm in length.

4.2. Twisting

Achieving and maximizing the twist. The objective is to actuate the structure so that the free edge twists but remains straight. For this purpose, n points are identified along the edge. The vertical displacement, v_i, $i = 1, n$, of each is to be controlled and maximized by selecting actuator strains ε_j, $j = 1, m$, for m independent actuators, where $m > n$. The redundancy among the actuators will be used to optimize the twist of the edge, within the force capabilities of the actuators: a crucial requirement for *actuator-limited* structures. From analysis or measurement of the actuation of the structure without passive loading, a matrix $\boldsymbol{A}$ of influence coefficients can be constructed such that

$$v_i = \sum_{j=1}^{m} A_{ij}\varepsilon_j. \tag{21}$$

Thus, $\boldsymbol{A}$ is an n by m matrix, with rank n. In some cases, the rank of $\boldsymbol{A}$ will be $r < n$, which implies that only r of the n controlled displacements will be linearly independent. This situation is undesirable, since the

displacements cannot be controlled independently and cannot be guaranteed to form a straight line upon twisting. In this case, control points should be dropped and n reduced until $r \to n$.

The null-space of the matrix $\boldsymbol{A}$ has dimension $m - n$ and consists of combinations of actuator strains that give rise to zero displacements at the control points along the edge to be twisted (Luenberger, 1973). An ortho-normal basis for the null-space is the set of $m - n$ vectors ε_j^k, $k = 1, m - n$, such that

$$\sum_{j=1}^{m} A_{ij}\varepsilon_j^k = 0. \tag{22}$$

These basis vectors ε_j^k can be found from Eq. (22) by standard matrix manipulations (Kreyszig, 1999). Now calculate

$$w^k = \sum_{j=1}^{m} \varepsilon_j^k \varepsilon_j, \tag{23}$$

which are projections of the actuator strain array into the null-space of $\boldsymbol{A}$. Therefore, w_k, $k = 1, m - n$, represent the degrees of freedom that lead to zero displacements of the control points. Now introduce a matrix $\boldsymbol{B}$ defined as

$$B_{ij} = \left\{ \begin{array}{ll} A_{ij}, & i = 1, n \\ \varepsilon_j^{i-n}, & i = n+1, m \end{array} \right\}. \tag{24}$$

Thus, $\boldsymbol{B}$ is m by m with the matrix $\boldsymbol{A}$ forming its first n rows and ε_j^k forming its lower $m - n$ rows. It follows from Eq. (24) that

$$\sum_{j=1}^{m} B_{ij}\varepsilon_j = \left\{ \begin{array}{ll} v_i, & i = 1, n \\ w^{i-n}, & i = n+1, m \end{array} \right\}. \tag{25}$$

Since all its rows are linearly independent, the matrix $\boldsymbol{B}$ is non-singular and inversion of Eq. (25) provides

$$\varepsilon_j = \sum_{i=1}^{n} B_{ji}^{-1} v_i + \sum_{i=n+1}^{m} B_{ji}^{-1} w^{i-n}. \tag{26}$$

The structure of Eq. (26) shows that a required twist can be achieved by specifying the n displacements v_i for the control points, plus any values for the remaining $m - n$ parameters w^k, because the latter do not affect on the control point displacements.

Now maximize the twist of the edge without exceeding the force limits of the actuators. Through analysis (or measurement) without passive loads, the relationship between the actuator forces P_k, $k = 1, q$, and the actuator strains ε_i, $i = 1, m$ can be established as

$$P_k = \sum_{i=1}^{m} C_{ki}\varepsilon_i. \tag{27}$$

Thus $\boldsymbol{C}$ is a q by m matrix with $q \geqslant m$. Note that q may be larger than m because actuators may be operated in pairs or sets to have the same actuator strain, but each actuator in general experiences different force levels, even when paired or put together in sets. Combining Eqs. (26) and (27) gives

$$P_k = \sum_{j=1}^{m} C_{kj} \left(\sum_{i=1}^{n} B_{ji}^{-1} v_i + \sum_{i=n+1}^{m} B_{ji}^{-1} w^{i-n} \right). \tag{28}$$

Expressing the control point displacements in terms of a single degree of freedom, ϕ, that represents the amount of twisting

$$v_i = \phi \bar{v}_i, \tag{29}$$

where $\bar{v}_i$ are simply the displacements of the control points for unit value of ϕ. As a result, Eq. (28) becomes

$$P_k = \beta_k \phi + \sum_{i=1}^{m-n} D_{ki} w^i, \tag{30}$$

where

$$\beta_k = \sum_{j=1}^{m} \sum_{i=1}^{n} C_{kj} B_{ji}^{-1} \bar{v}_i, \tag{31}$$

and $\boldsymbol{D}$ is a m by $m-n$ matrix given by

$$D_{ki} = \sum_{j=1}^{m} C_{kj} B_{ji+n}^{-1}. \tag{32}$$

The remaining task is to maximize ϕ in Eq. (30) subject to minimum and maximum constraints on the actuator forces P_k. This is a straightforward linear programming problem (Luenberger, 1973) to find the $m-n$ coordinates w^i. Once solved, the resulting values of ϕ and w^i are inserted into Eqs. (29) and (26) to compute the required actuator strains that produce the maximum possible twisting within the actuator force constraints.

Illustrations relevant to the current demonstration. The demonstration structure has eight independently operated actuators (Fig. 3). Five points are chosen on the actuated edge as control points (thus $n = 5$ and $m = 8$). Finite element calculations have provided the following results for the matrix $\boldsymbol{A}$ with the displacement of the control points measured in mm:

$$[A] = \begin{pmatrix} 15.60 & -17.76 & 168.32 & 26.76 & 93.32 & -9.17 & 56.33 & -8.03 \\ 2.73 & 4.27 & 111.99 & 24.70 & 112.99 & 19.97 & 50.00 & -1.22 \\ 2.95 & 69.66 & 49.66 & 41.33 & 41.33 & 48.66 & 69.66 & 2.93 \\ -1.22 & 50.00 & 19.93 & 112.66 & 24.80 & 112.32 & 4.23 & 2.68 \\ -8.13 & 56.33 & -9.20 & 92.99 & 26.90 & 168.65 & -17.66 & 15.50 \end{pmatrix}, \tag{33}$$

which has rank 5 as required. The null space of $\boldsymbol{A}$ has dimension 3 and its base vectors are

$$\begin{aligned} \{\varepsilon^1\}^{\mathrm{T}} &= \{\, 36.10 \quad -0.68 \quad -6.18 \quad -0.35 \quad 5.17 \quad 1.00 \quad 0.00 \quad 0.00 \,\}, \\ \{\varepsilon^2\}^{\mathrm{T}} &= \{\, -0.07 \quad -0.99 \quad -0.35 \quad 0.14 \quad -0.15 \quad 0.36 \quad 1.00 \quad 0.00 \,\}, \\ \{\varepsilon^3\}^{\mathrm{T}} &= \{\, 0.01 \quad -0.03 \quad 0.01 \quad 0.15 \quad -0.01 \quad -0.16 \quad 0.01 \quad 1.00 \,\}. \end{aligned} \tag{34}$$

Note that these expressions have not been normalized, so strictly, ε_j^i do not form an ortho-normal basis. However, the two basis vectors are orthogonal, which suffices for our purposes. The matrix $\boldsymbol{B}$ then becomes

$$[B] = \begin{pmatrix} 15.60 & -17.76 & 168.32 & 26.76 & 93.32 & -9.17 & 56.33 & -8.03 \\ 2.73 & 4.27 & 111.99 & 24.70 & 112.99 & 19.97 & 50.00 & -1.22 \\ 2.95 & 69.66 & 49.66 & 41.33 & 41.33 & 48.66 & 69.66 & 2.93 \\ -1.22 & 50.00 & 19.93 & 112.66 & 24.80 & 112.32 & 4.23 & 2.68 \\ -8.13 & 56.33 & -9.20 & 92.99 & 26.90 & 168.65 & -17.66 & 15.50 \\ 36.10 & -0.68 & -6.18 & -0.35 & 5.17 & 1.00 & 0.00 & 0.00 \\ -0.07 & -0.99 & -0.35 & 0.14 & -0.15 & 0.36 & 1.00 & 0.00 \\ 0.01 & -0.03 & 0.01 & 0.15 & -0.01 & -0.16 & 0.01 & 1.00 \end{pmatrix}, \tag{35}$$

and its inverse is

$$[B]^{-1} = \begin{pmatrix} 4.23 & -5.17 & 1.09 & -1.18 & 1.23 & 26.36 & -29.37 & 8.61 \\ -2.89 & -0.99 & 9.06 & -0.92 & -1.14 & -0.50 & -434.19 & -20.87 \\ 14.59 & -12.77 & 1.65 & -6.51 & 6.54 & -4.51 & -154.95 & 12.92 \\ -4.65 & 4.29 & -5.13 & 22.35 & -14.16 & -2.55 & 59.44 & 142.36 \\ -14.04 & 22.24 & -5.13 & 4.31 & -4.68 & 3.78 & -64.10 & -9.71 \\ 6.53 & -6.50 & 1.60 & -12.75 & 14.59 & 0.73 & 158.47 & -152.17 \\ -1.21 & -0.83 & 9.00 & -1.08 & -2.78 & 0.00 & 437.97 & 8.86 \\ 1.28 & -1.26 & 1.15 & -5.25 & 4.29 & 0.00 & 0.00 & 953.00 \end{pmatrix} \times 10^3. \quad (36)$$

There are a total of eight actuators so that $q = 8$. The matrix $\boldsymbol{C}$ was determined by finite element analysis to be

$$[C] = \begin{pmatrix} -27.50 & 14.06 & 25.53 & 11.33 & -13.20 & -9.47 & 6.10 & -9.33 \\ 13.97 & -320.97 & 98.66 & 123.65 & -18.26 & 56.99 & 36.00 & 6.00 \\ 24.70 & 97.99 & -295.64 & -14.60 & 202.31 & -70.67 & 55.99 & -10.20 \\ 10.57 & 122.99 & -14.50 & -343.30 & 44.00 & 202.31 & -18.56 & -13.87 \\ -13.97 & -18.93 & 202.65 & 44.00 & -343.30 & -14.10 & 122.65 & 10.43 \\ -10.30 & 55.99 & -70.66 & 201.98 & -14.17 & -295.30 & 97.66 & 24.46 \\ 5.97 & 36.00 & 56.66 & -17.93 & 123.32 & 98.32 & -320.30 & 13.93 \\ -9.33 & 6.13 & -9.33 & -13.10 & 11.20 & 25.30 & 14.03 & -27.36 \end{pmatrix}, \quad (37)$$

where the load is measured in MPa. Thus the inner product of $\boldsymbol{C}$ and $\boldsymbol{B}^{-1}$ is

$$[C][B]^{-1} = \begin{pmatrix} 0.27 & -0.37 & 0.18 & 0.21 & -0.18 & -0.91 & -6.57 & -6.00 \\ 2.44 & -1.30 & -2.85 & 1.52 & 0.12 & 0.02 & 156.98 & 26.45 \\ -7.81 & 8.41 & -0.16 & 3.24 & -3.98 & 2.65 & 2.03 & -9.15 \\ 1.78 & -1.77 & 2.78 & -10.00 & 7.38 & 0.68 & -50.76 & -97.36 \\ 7.34 & -9.96 & 2.78 & -1.79 & 1.81 & -2.59 & 53.33 & 25.85 \\ -3.99 & 3.26 & -0.15 & 8.40 & -7.81 & -0.30 & -4.18 & 95.28 \\ 0.15 & 1.48 & -2.82 & -1.26 & 2.40 & 0.43 & -158.25 & -8.60 \\ -0.18 & 0.21 & 0.18 & 0.37 & 0.27 & -0.14 & 7.72 & -32.17 \end{pmatrix}. \quad (38)$$

The optimization as carried out for a twisting motion defined by

$$\begin{pmatrix} v_1 \\ v_2 \\ v_3 \\ v_4 \\ v_5 \end{pmatrix} = \phi \begin{pmatrix} 0.00 \\ 0.25 \\ 0.50 \\ 0.75 \\ 1.00 \end{pmatrix}, \quad (39)$$

so that one corner moves upward and the other downwards. With this motion

$$\{\beta\}^{\mathrm{T}} = \{\, 0.409 \quad 0.0471 \quad 0.148 \quad -0.339 \quad 0.344 \quad -0.345 \quad -0.154 \quad -0.392 \,\}, \quad (40)$$

and $\boldsymbol{D}$ is the 8 by 3 matrix formed by the three rightmost columns of Eq. (38). The constraints on the actuators are that the stress carried by each must lie between −0.4 and 0.4 MPa. With these restrictions, optimization of ϕ using Mathematica provides the results

$$\begin{pmatrix} w_1 \\ w_2 \\ w_3 \end{pmatrix} = \begin{pmatrix} -1.002 \\ 0.131 \\ 0.0464 \end{pmatrix}, \quad (41)$$

with $\phi = 6.64$ mm. Thus, within the limits of the actuators, the optimized twisting involves a motion in which one corner is displaced by 6.8 mm relative to the other. Twisting is more limited than hinging because of the associated stretching of the solid face sheet. Note, however, that the realizable twist scales linearly with the force capacity of the actuator (provided that the face does not yield). Accordingly, incorporation of an actuator with factor 6 higher capacity (to achieve the structure-limited hinging described above) would allow a twist of almost 7 cm.

5. The demonstration

5.1. Assembly

A detailed description of the processes used to manufacture the foregoing structure (Fig. 3(a)) is provided elsewhere (Maxwell et al., 2003). The Kagome face members have square cross-section (1.5×1.5 mm), while the core members are rectangular (0.75×1.5 mm), with unit length 51 mm. Stainless steel 304 was used for the Kagome back-plane and the core. The stiffness-matched solid face comprised polycarbonate, thickness 1.5 mm. After assembly, eight of the Kagome members were removed and replaced with the linear stepper motors. The entire assembly was rigidly attached to three heavy L-shaped stainless steel supports. The polycarbonate face was reinforced with an aluminum stripe. The fully assembled structure is shown in Fig. 3(b).

A computer based system is devised to control the actuators. Every actuator is connected to a drive card (Haydon Switch, model 39105) which distributes the power from an attached DC power supply to the motors in the correct stepping sequence. All drive cards are connected through a digital interface (Keithley KPCI-3102) to the control computer. The drive cards are controlled by two digital signals, determining the direction of the actuation and the stepping. A custom designed program stores the position of every actuator and coordinates the actuators to obtain the desired shape by generating the direction and the stepping signals.

5.2. Comparison with model

To demonstrate hinging subject to a small (1 kg) restraining load, all actuators were extended simultaneously by 7% (equivalent to 281 steps at 12.7 μm/step). A 23 mm tip displacement was realized, in good agreement with the FEM simulation (26 mm). The present actuators have a load limit of ~50 N at a stepping rate of 50/s, resulting in the maximum allowable load capacity summarized on Fig. 9. Verification of this estimate was performed by sequentially elevating the load on the free edge by 0.5 kg until the actuators ceased operation. This procedure revealed that the actuation became erratic (but did not cease entirely) at loads exceeding 3.0 kg. This load capacity compares well with the calculated value of 2.5 kg. Recall that a load of 30 kg could be lifted if the system were not actuator limited. Measurement repeated with a 50 μm thick Al alloy face sheet did not change the results.

Demonstration of the twisting mode was based on the actuator strains provided by the optimization procedure described in Section 4.2. These strains were, respectively, −2.91%, 0.97%, −0.17%, 1.50%, 0.52%, 2.22%, 1.08% and 4.83% for the eight actuators. The maximum twist that could be corresponded to a 6.5 mm height difference between the two edges, in close agreeing the predicted value (6.8 mm). Recall that larger twist angles would be possible with superior actuators. The final shapes of the demonstration structure for the hinging and twisting modes are shown in Fig. 13.

This comparison has achieved two primary objectives:

(i) It has affirmed that the structure in its present form is actuator-limited, highlighting the need for superior actuators that allow the system to realize its potential. Assessments of alternative actuators are in progress.

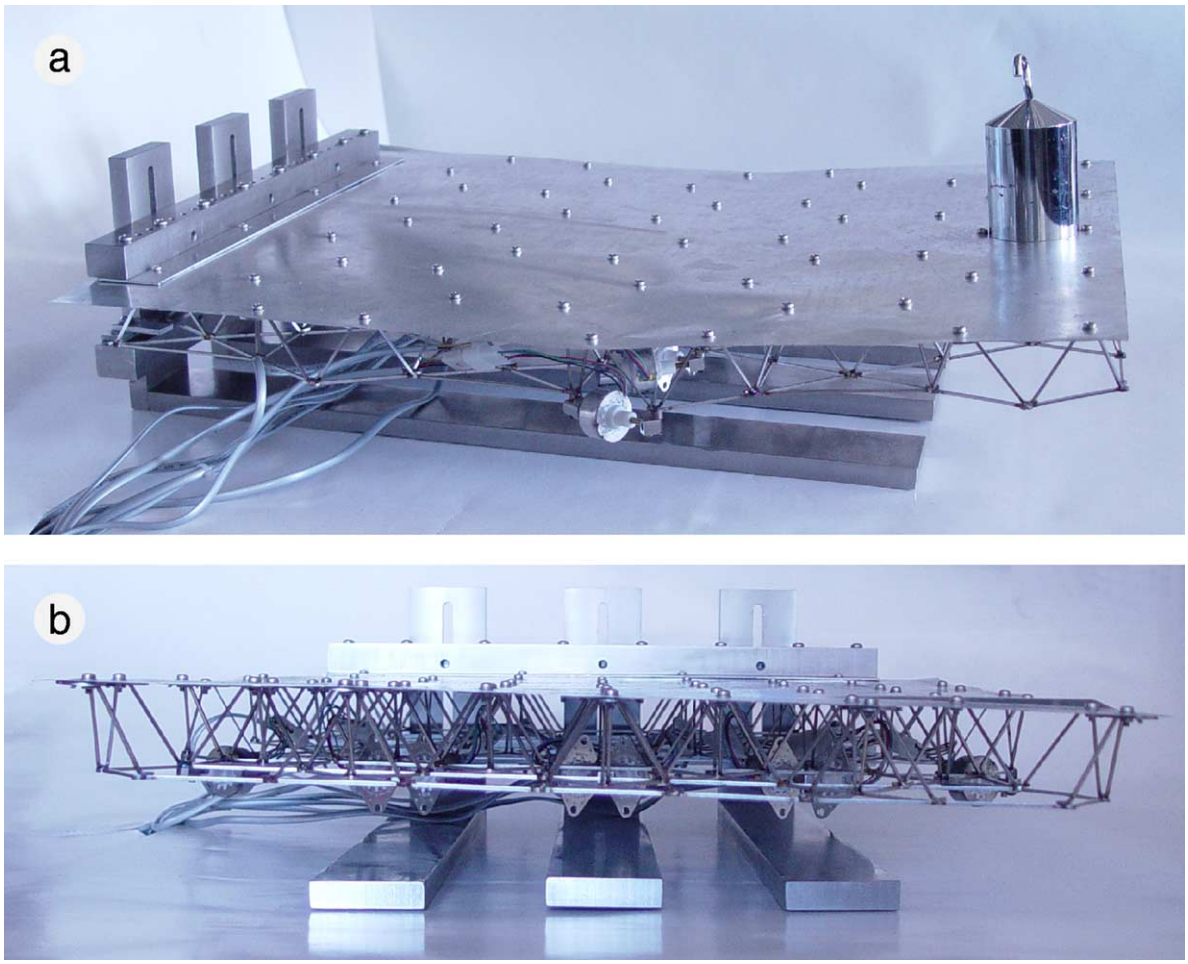

Fig. 13. Demonstration of the hinging and twisting modes when an Al alloy face sheet is used.

(ii) The agreement between measured and calculated displacements and load capacities has provided confidence in the numerical method, allowing the method to be used to set objectives for ongoing activities related to alternative materials, as well as structural and actuator enhancements.

6. Concluding remarks

A combination of analytical and numerical assessments has been used to guide the design of a high authority shape morphing structure, based on the attributes of a Kagome active plane. A version of the structure has been manufactured using a stainless steel active face and core, with a polycarbonate passive face, and commercially available linear stepper actuators. Hinging and twisting has been demonstrated. It has not been possible to demonstrate the full capabilities of the system because of the limitations imposed by the actuators. These limitations have been characterized in a consistent manner, using both measurements and simulations, allowing the numerical method to be used to set the objectives that need to be realized to demonstrate the full potential.

The scaling used in conjunction with numerical simulations has identified the following objectives.

(i) Among potential material candidates, Ti–6V–4Al appears to be the best choice, because of its high yield strain and relatively low density. The replacement of steel by this alloy will eliminate fatigue in hinging actuations and allow the passive load capacity to increase to 4.8 kN/m at lower overall weight. It will also slightly increase the load that can be lifted by the present actuators and increase the realizable twisting angle. Such a system is being fabricated by diffusion bonding.
(ii) New capability is needed for linear actuators that allow the system to become structure-limited. For a Ti system, to realize the full authority potential in a hinging mode, the maximum force capacity would need to be increased to 1200 N (compared with 50 N for the present actuators), while still capable of strains of order 10% at acceptable frequencies. Such a capacity would also permit extensive twisting. New developments in piezoelectric and ferromagnetic shape memory systems will provide the much greater authority needed to obviate these limitations (Karaca et al., 2003).
(iii) The incorporation of fully flexible joints at the core members encompassing the actuation sites would reduce the forces on the actuators and eliminate any tendency for fatigue.

It will be important to compare and contrast the performance of the present structure with that comprising two Kagome faces and a tetrahedral core (Symons et al., 2003). This comparison will establish the circumstances governing the choice between these complementary designs.

Appendix A. Scaling of the actuation resistance to hinging

The scaling of the actuation resistance of the demonstration structure (Fig. 3) can be ascertained from analysis of the two-dimensional structure shown in Fig. 14(a). The configuration consists of a face sheet having elastic bending stiffness $E_{\mathrm{pf}}I_{\mathrm{pf}}$ (where I_{pf} is the second moment of area of its cross-section), bonded to symmetrically triangulated core members with bending stiffness $E_{\mathrm{c}}I_{\mathrm{c}}$. An actuator (not shown), attached to the structure by pin-joints, applies a force F_{A} to each apex of the core members. The ensuing displacement, $\Delta/2$, is a measure of the actuation resistance of the structure, $k = F_{\mathrm{A}}/\Delta$. The response is dominated by elastic bending of both the face sheet and the core members. Elastic extension of each component leads only to a negligible, higher order, correction. Accordingly, the stiffness in local coordinates of a core member, with nodes A and B (Fig. 14(b)) is (Thomson and Dahleh, 1998):

$$\begin{Bmatrix} F_2^A \\ M^A \\ F_2^B \\ M^B \end{Bmatrix} = \frac{E_{\mathrm{c}}I_{\mathrm{c}}}{L^3} \begin{bmatrix} 12 & 6L & -12 & 6L \\ 6L & 4L^2 & -6L & 2L^2 \\ -12 & -6L & 12 & -6L \\ 6L & 2L^2 & -6L & 4L^2 \end{bmatrix} \begin{Bmatrix} u_2^A \\ \theta^A \\ u_2^B \\ \theta^B \end{Bmatrix}, \tag{A.1}$$

where u_i^N, $i = 1, 2$, $N = A, B$, are the displacement components of the nodes, θ^N, $N = A, B$, are the anti-clockwise nodal rotations, F_i^N, $i = 1, 2$, $N = A, B$, are the applied force components at the nodes and M^N, $N = A, B$, are the applied nodal moments, positive when anti-clockwise. Equilibrium requires that

$$F_1^A + F_1^B = 0, \tag{A.2}$$

and inextensibility provides

$$u_1^B = u_1^A. \tag{A.3}$$

Equivalent relationships are valid for a face sheet member with $E_{\mathrm{c}}I_{\mathrm{c}}$ and L in Eq. (A.1) replaced by $E_{\mathrm{pf}}I_{\mathrm{pf}}$ and $\sqrt{2}L$, respectively.

The solution procedure seeks three equilibrium equations that contain the load, F_{A}, the bending moments, M, and shear forces, V, by eliminating the member tensions, T (Fig. 14(c)):

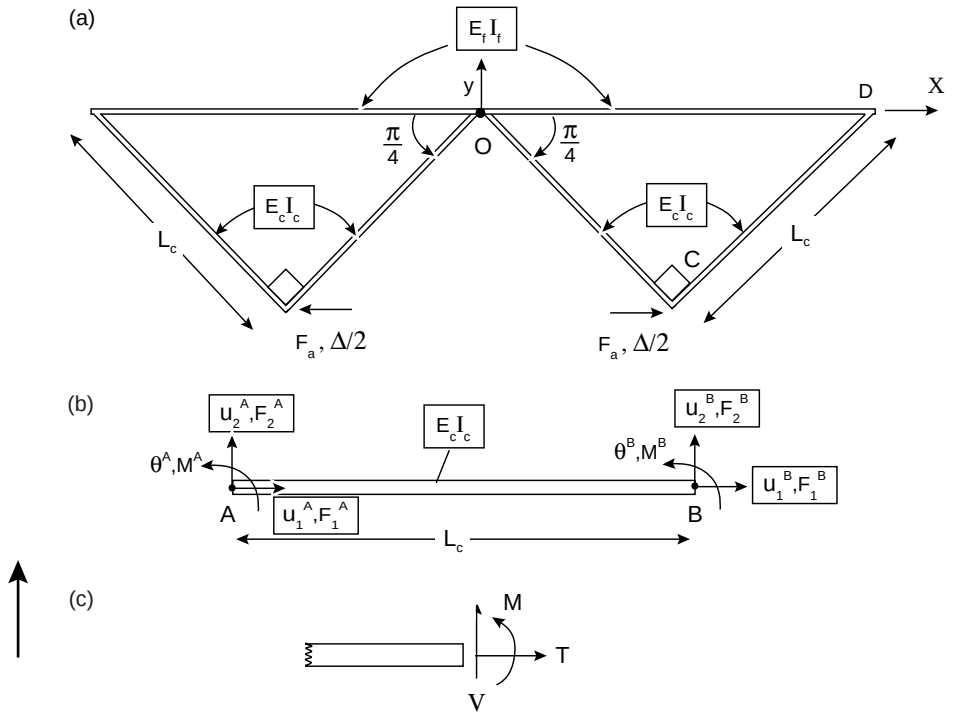

Fig. 14. Two-dimensional structure used to determine the actuation resistance. (a) Full model consisting of the face sheet and two core units. (b and c) Nomenclature describing the core members.

$$\begin{aligned} &M_{CD} + M_{OD} = 0, \\ &M_{OC} - M_{CD} - V_{CD}L = 0, \\ &F_{\mathrm{A}} = \sqrt{2}(V_{OC} + V_{CD}) + 2V_{OD}, \end{aligned} \tag{A.4}$$

where M_{AB} and V_{AB} are the bending moment and shear force, respectively, at the right-hand end of member AB (Fig. 14(b)).

Since the point O at the origin (Fig. 14(a)) neither displaces nor rotates, it can be deduced from inextensibility that joint C moves a distance $\Delta/\sqrt{2}$ towards point D and joint D moves a distance Δ in the direction parallel to the positive y-axis. Use of Eq. (A.1) for the relevant members then provides

$$\begin{aligned} M_{OC} &= \frac{E_{\mathrm{c}}I_{\mathrm{c}}}{L^3}\left(4L^2\theta_C - \frac{6L}{\sqrt{2}}\Delta\right), \\ V_{OC} &= \frac{E_{\mathrm{c}}I_{\mathrm{c}}}{L^3}\left(6\sqrt{2}\Delta - 6L\theta_C\right), \\ M_{CD} &= \frac{E_{\mathrm{c}}I_{\mathrm{c}}}{L^3}\left(2L^2\theta_C + 4L^2\theta_D - \frac{6L}{\sqrt{2}}\Delta\right), \\ V_{CD} &= \frac{E_{\mathrm{c}}I_{\mathrm{c}}}{L^3}\left(6\sqrt{2}\Delta - 6L\theta_C - 6L\theta_D\right), \\ M_{OD} &= \frac{E_{\mathrm{pf}}I_{\mathrm{pf}}}{L^3}\left(2\sqrt{2}L^2\theta_D - 3L\Delta\right), \\ V_{OD} &= \frac{E_{\mathrm{pf}}I_{\mathrm{pf}}}{L^3}\left(3\sqrt{2}\Delta - 3L\theta_D\right), \end{aligned} \tag{A.5}$$

where θ_C and θ_D are the anti-clockwise rotations of joints C and D, respectively.

The first two of equations of (A.4) give

$$\theta_C = \frac{9(\sqrt{2}E_cI_c + E_{pf}I_{pf})\Delta}{2(7E_cI_c + 4\sqrt{2}E_{pf}I_{pf})L}, \tag{A.6}$$

and

$$\theta_D = \frac{3\sqrt{2}(E_cI_c + \sqrt{2}E_{pf}I_{pf})\Delta}{(7E_cI_c + 4\sqrt{2}E_{pf}I_{pf})L}. \tag{A.7}$$

These two results are inserted into the first of Eq. (A.4) to provide the actuation resistance

$$k = \frac{F_A}{\Delta} = \frac{6\sqrt{2}(E_cI_c + \sqrt{2}E_{pf}I_{pf})(2\sqrt{2}E_cI_c + E_{pf}I_{pf})}{(7E_cI_c + 4\sqrt{2}E_{pf}I_{pf})L^3}. \tag{A.8}$$

For a system, width w, with n core members

$$I_c = \frac{n}{12}d_c^4, \tag{A.9}$$

and

$$I_f = \frac{w}{12}d_{pf}^3, \tag{A.10}$$

such that Σ (as defined in Eq. (17b)) becomes

$$\Sigma = \frac{\left(n + \sqrt{2}\frac{E_{pf}}{E_c}\alpha\right)\left(2\sqrt{2}n + \frac{E_{pf}}{E_c}\alpha\right)\left(\frac{L_c}{L}\right)^3}{\sqrt{2}\left(7n + 4\sqrt{2}\frac{E_{pf}}{E_c}\alpha\right)}. \tag{A.11}$$

Generalization to account for the three-dimensionality of the demonstration structure and its heterogeneity in elastic properties yields Eq. (17a).

References

Ashby et al., 2000. Metal Foams: A Design Guide. Butterworth–Heinemann, Boston.

Christensen, R.M., 2000. Mechanics of cellular and other low-density materials. Int. J. Solids Struct. 37, 93–104.

Deshpande, V., Fleck, N.A., 2001. Int. J. Solids Struct. 38, 62–75.

Hutchinson, R.G., Wicks, N., Evans, A.G., Fleck, N.A., Hutchinson, J.W., 2003. Kagome plate structures for actuation. Int. J. Solids Struct. 40, 6969–6980.

Hyun, S., Torquato, S., 2002. Optimal and manufacturable two-dimensional, Kagomé-like cellular solids. J. Mater. Res. 17, 137–144.

Karaca, H.E., Karaman, I., Lagoudas, D.C., Maier, H.J., Chumlyakov, Y.I., 2003. Recoverable stress-induced martensitic transformation in a ferromagnetic CoNiAl alloy. Scripta Mater. 49, 831–836.

Kreyszig, E., 1999. Advanced Engineering Mathematics, eighth ed. Wiley, New York.

Luenberger, D.G., 1973. Linear and Nonlinear Programming, second ed. Addison-Wesley, Reading, MA.

Lu, T.J., Hutchinson, J.W., Evans, A.G., 2001. Optimal design of a flexural actuator. J. Mech. Phys. Solids 49, 2071–2093.

Maxwell, P., dos Santos e Lucato, S.L., Evans, A.G., 2003. Fabrication of a high-authority Kagome actuator, to be submitted.

Symons, D., Hutchinson, R.G., Fleck, N.A., 2003. Actuation performance of the Kagome Double Layer Grid. Submitted to J. Mech. Phys. Solids.

Thomson, W.T., Dillon Dahleh, M., 1998. Theory of Vibration with Applications, fifth ed. Prentice-Hall, Englewood Cliffs, NJ.

Wicks, N., 2003. Optimization and actuation of truss structures. Ph.D. Thesis, Engineering Sciences, Harvard University, Cambridge, Massachusetts.

Wicks, N., Hutchinson, J.W., 2001. Optimal truss plates. Int. J. Solids Struct. 38, 5165–5183.